Phase Separation and Development of the Microstructure for Stainless Steel to Copper Alloy Weld Joints Using a Fiber Laser

Sheila Medeiros de Carvalho[1], Rafael Humberto de Mota Siqueira[1], Milton Sergio Fernandes de Lima[1,*]

Carvalho SM (iD) https://orcid.org/0000-0003-4583-9451
Siqueira RHM (iD) https://orcid.org/0000-0003-4581-2005
Lima MSF (iD) https://orcid.org/0000-0001-5540-8802

ABSTRACT: Stainless steel and copper alloys joints are often applied in aerospace, marine and power industries where both high thermal and electrical conductivity (Cu) and corrosion resistance (steel) are required. In the aerospace industry, in particular for the combustion chamber of rocket engines, copper and steel combinations offer perfect materials selection due to their combined high thermal conductivity and good stiffness. In this work, laser welds were produced with intensity between 3.8 × 104 and 5.7 × 104 W/mm² and a heat input between 72 and 108 J/mm, giving an aspect ratio of 1.8. The microstructure of the weld beads was marked by chemical heterogeneities due to the phase separation between Cu and Fe in the liquid state. The phase separation gave rise to globular precipitates which further transform due to a secondary precipitation at temperatures below 1000 °C. The steel side part of the weld presents around 20% Cu, leading to a liquation of the grain boundaries and cracking at high heat inputs. The hardness values situated between both base materials and the tensile shear behavior, when the weld is sufficiently tough, present strength up to 350 MPa and elongation up to 10%.

KEYWORDS: Welding, Copper alloys, Laser.

INTRODUCTION

Stainless steel and copper alloys joints are often applied in aerospace, marine and power industries where both high thermal and electrical conductivity (Cu) and corrosion resistance (steel) are required. Although the evident advantages, the weldability of these very dissimilar metals is a challenge due to differences in their physical properties, as well as the solutes heterogeneity (Meng *et al.* 2019). A given method to avoid the solidification cracks requires particular attention as well (Noecker and DuPont 2007; Kuryntsev *et al.* 2017). Usually, these cracks result from the combined effect of segregation of copper to the grain boundaries of steel and to the presence of residual stresses (Kuryntsev *et al.* 2017).

In the aerospace industry, in particular for the combustion chamber of rocket engines, copper and steel combinations offer perfect materials selection due to their combined high thermal conductivity and good stiffness (Velu and Bhat 2015). The high thermal conductivity of copper tends to rapidly dissipate heat from the hot gases inside the combustor. The high steel stiffness gives to the component a lightweight and environment corrosion resistance. On the other hand, this type of weld is one of the most difficult to be realized using these materials: superposed with steel at the top.

Concerning the composition modulations in the welds, the solidification of Fe-Cu alloys at high cooling rates, such as resolidification after laser beam welding, induces dynamic bulk melt supercooling. The occurrence of melt separation also depends on alloy composition (Wang *et al.* 2017). This behavior promotes the liquid metal entering a metastable liquid miscibility gap. As liquid phase separation occurs well below *liquidus* and separate into two liquids: an iron-rich melt (L1), and a copper-rich melt (L2), as illustrated in binary Cu-Fe phase diagram in Fig. 1 (Munitz 1995). This molten phase separation may negatively influence the mechanical behavior of the welds.

Chen *et al.* (2015) studied the influence of process variables, such as welding speed, laser power, standoff distance and inclination on the stainless steel to copper laser butt welds. They observed that the offsetting and the inclination of the laser beam in the direction of the stainless steel could effectively minimize the copper melting and ensure the joining occurs via brazing. In the laser brazing mode, there is a formation of a metallurgical bonding between the stainless steel and the copper. The tensile strength remained approximately unchanged with an increasing of laser beam offset, but, when the offset exceeds 0.3 mm, there is an incomplete fusion and the tensile strength decreased.

Figure 1. Fe-Cu phase diagram (Munitz 1995).

Mai and Spowage (2004) had characterized the copper-steel butt joint laser welds. They used a 350 W pulsed Nd:YAG laser focusing 0.2 mm into the steel plate. They observed a very limited amount (approx. 2%) of copper dissolved in the molten steel and no cracks in the weld were observed. Nevertheless, an incomplete metallurgical bond was obtained at the interface between the Cu-plate and the weld metal leading to an inconsistent mechanical behavior.

Magnabosco *et al.* (2006) investigated three different welded joints produced by electron beam welding. The first joint was obtained between plates of copper C11000 and AISI 304L steel. The second joint was obtained between a plate of C11000 and AISI 304. The last one was obtained between a plate of copper C 18100 and AISI 316L. Due to the high thickness of specimens 2 and 3, a two pass was chosen in order to solve the limited heat input issue. The first specimen did not reveal defects. But the other two showed porosity in the copper-rich phase and intergranular cracks at the interface between the fusion zone and the base stainless steel. This investigation demonstrated that this kind of welding might be very dependent on the strict control of process variables such as weld power, number of runs and weld speed.

The aim of this study is to investigate laser beam weld of copper C18200 and steel AISI 304 in the lap joint configuration for possible application in the space industry considering both microstructure and mechanical behavior.

MATERIALS AND METHODOLOGY

Sheets of copper class C18200 previously solution and aging heat treated (90 mm × 50 mm × 2.05 mm) and stainless steel AISI 304L (90 mm × 50 mm × 0.75 mm) were used as start materials. Tables 1 and 2 summarize their measured chemical compositions and mechanical properties, respectively, used in this work. The symbols YS, UTS and EL in Table 2 are 0.2% yield strength, ultimate tensile strength and elongation at break, respectively.

Table 1. Chemical compositions of the starting materials (wt. %).

Material	Fe	C	Mn	Si	Cr	Ni	Cu	Zr	Zn
AISI 304	Bal.	0.07	2.00	0.75	17.5-19.5	8.0-10.5			
C18200	0.02				0.704	0.005	Bal.	0.072	0.032

Table 2. Mechanical properties at 27 °C.

Material	YS (MPa)	UTS (MPa)	EL [%]
AISI 304	280	600	58
C 18200	450	460	4

An ytterbium fiber laser with 2 kW power (IPG, Model YLR-2000) was used with a head focal distance of 160 mm and a tilt angle of 2°. The plates were polished with grade 600 SiC paper. After, the samples were clamped in a lap-joint weld geometry (Fig. 2). The focal spot had a diameter of 200 μm. All welded condition was obtained by a single-run. Pure Argon with 8.0 L/min flow was used as protective gas for all experiments using a rounded nozzle 3 mm behind the fusion zone. As shown in Fig. 2, it is expected a heterogeneous weld due to the partial miscibility in the liquid state, such as an iron rich (Fig. 2, region 1) and copper rich (Fig. 2, region 2) solids.
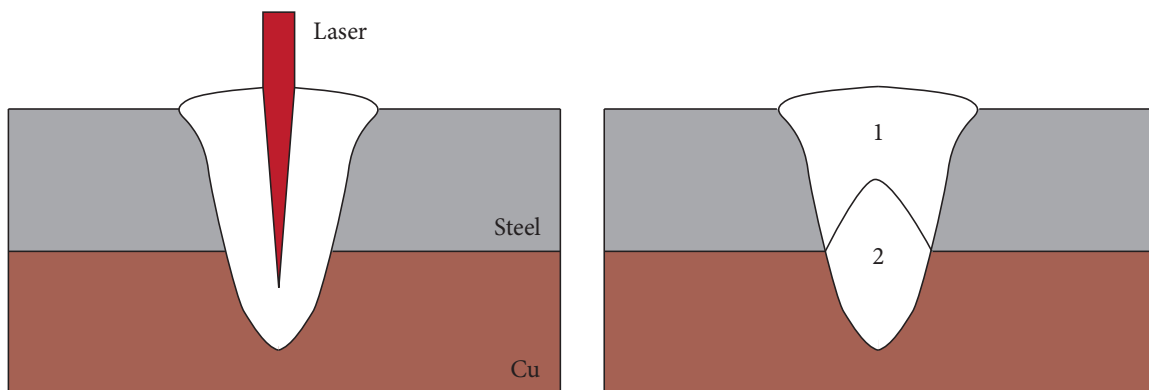
Figure 2. Schematics of lap joint welding by laser. Region 1 = Iron-rich side; Region 2 = Cu-rich side.

Table 3 shows the welding parameters. The welding speed was fixed at 1 m/min and the beam spot diameter was 0.2 mm on the steel surface. Table 3 also presents the heat input as the ratio between laser power and welding speed, and the intensity as the ratio between laser power and beam area.

Table 3. Laser welding parameters.

Parameters	Conditions			
	1	2	3	4
Power (W)	1,200	1,400	1,600	1,800
Heat input (J/mm)	72	84	96	108
Intensity (W/mm^2)	3.8×10^4	4.5×10^4	5.1×10^4	5.7×10^4

The microstructures of the joints were observed using a light optical microscope ZEISS model Imager2m and a scanning electron microscope (SEM) model MIRA3-TESCAN equipped with an energy-dispersive X-ray spectrometry (EDS) after standard grinding, polishing, and etching using a solution of iron chloride (5 vol.%. $FeCl_3$ + 50 vol.%. HCl + 45 vol.%. H_2O) for 10 s. A thermodynamics database FEDAT of ThermoCalc Software (Andersson *et al.* 2002) was used to study the phase balance of the welds.

The tensile strengths of the joints were evaluated at room temperature using an Instron EMIC DL10000 machine at a crosshead speed of 1.0 mm/min. The Vickers hardness profiles with a load of 50 gf and indentation time of 10 s were generated across the transversal section of the weld bead.

RESULTS AND DISCUSSION
MICROSTRUCTURAL ANALYSES

Figure 3 shows macrographies of the welds cross sections for the conditions listed in Table 3. The keyhole, characterized by a vapor channel into the melt pool, could be clearly seen in all conditions. The aspect ratios, as the depth per the top diameter, did not change appreciably within the heat input range and are situated around 1.8. The melt depth situated between 0.6 and 0.7 mm.

As can be seen in Fig. 3, the weld could be divided in two regions after etching, one light gray representing Fe-rich zone and a dark gray zone near to the Cu phase. Therefore, it could be foreseen a partial dissolution between the materials, but with limited chemical homogeneity in the fusion zone. The chemical heterogeneity has been expected since the welding speed (1 m/min) together with different liquid densities allows low dilution between Fe and Cu melts. In addition, as previously discussed, the Fe-Cu phase diagram presents a miscibility gap (Fig. 1).

Figure 4a shows a SEM micrograph of the weld under condition 1. As can be seen, there are two different HAZ and FZ in the AISI 304 side. The time involved in homogenization is quite short due to the rapid solidification. Considering an average liquid bath of about 0.6 mm and the welding speed of 1 m/min, the laser interaction time was about 0.036 s. The homogenization will thus be incomplete, although Marangoni convection may occur, and the weld presents two distinctive regions, Cu-rich and Fe-rich. Those regions are clearly seen in Fig. 4. During the miscibility gap period, a large range of possible micro-constituents may occur. After a period of an almost homogeneous liquid in a given region, a phase separation followed by secondary precipitation gave rise to second-phase decorated globules.

One possible way to understand phase transformation in the welds is though the close examination of FZ and HAZ. Next to the steel fusion zone, Fig. 4b, the epitaxial growth is followed by a dendritic growth. Since very little Cu is present here, the microstructure seems a homogenous steel fusion line. Near to the middle of the weld bead, Fig. 4c, Fe-rich and Cu-rich coexist, and then an epitaxial grown steel is followed by Cu-rich *globuli*. When the fusion line is well below the joint line and bounding the Cu-alloy, Fig. 4d, the weld is characterized by an almost fully Cu-based microstructure.

The globular genesis and development could be better studied by a close image using SEM, Fig. 5. Due to the different electrical conductivities, copper appears light gray in SEM compared to the dark gray of Fe-rich phases. Floating Cu globules in the iron melt, such as those presented in Figs. 5a and 5b, decomposes to Fe-rich precipitates in solid-state as presented by the arrow in Fig. 5b. The Cu-rich regions (Figs. 5c and 5d) also present decomposition during cooling, but as Cu has a smaller melting point, the Cu precipitates in Fe globules has spherical shape, indicating a later solidification (arrow in Fig. 5d). Away from the globules, the matrices also present secondary precipitation.
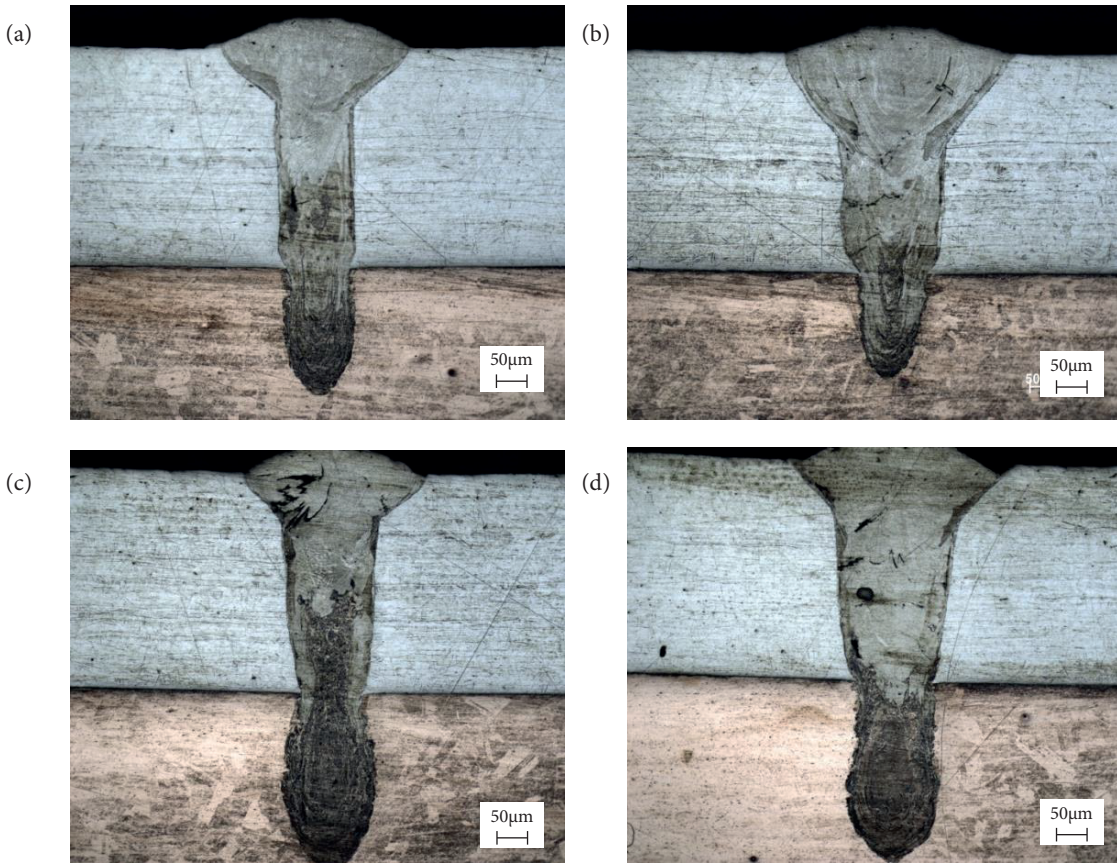
Figure 3. Copper–steel welded macrostructure by using laser focused on the steel surface with different laser powers: (a) 1200 W; (b) 1400 W; (c) 1600 W; and (d) 1800 W.
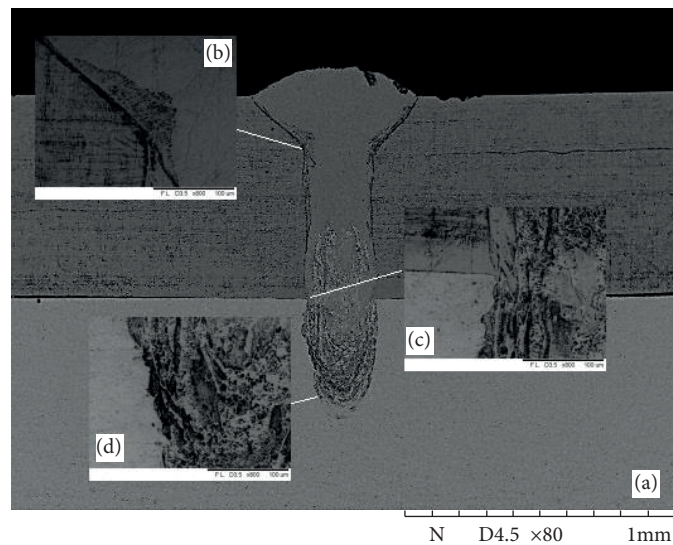

Figure 4. SEM micrograph showing the welding region of condition 1200 W and 1/min. The photographic details are representative of the different microstructural regions: (a) General view; (b) Detail of the steel diffusion; (c) Interface between the materials; and (d) Bottom line segregation.
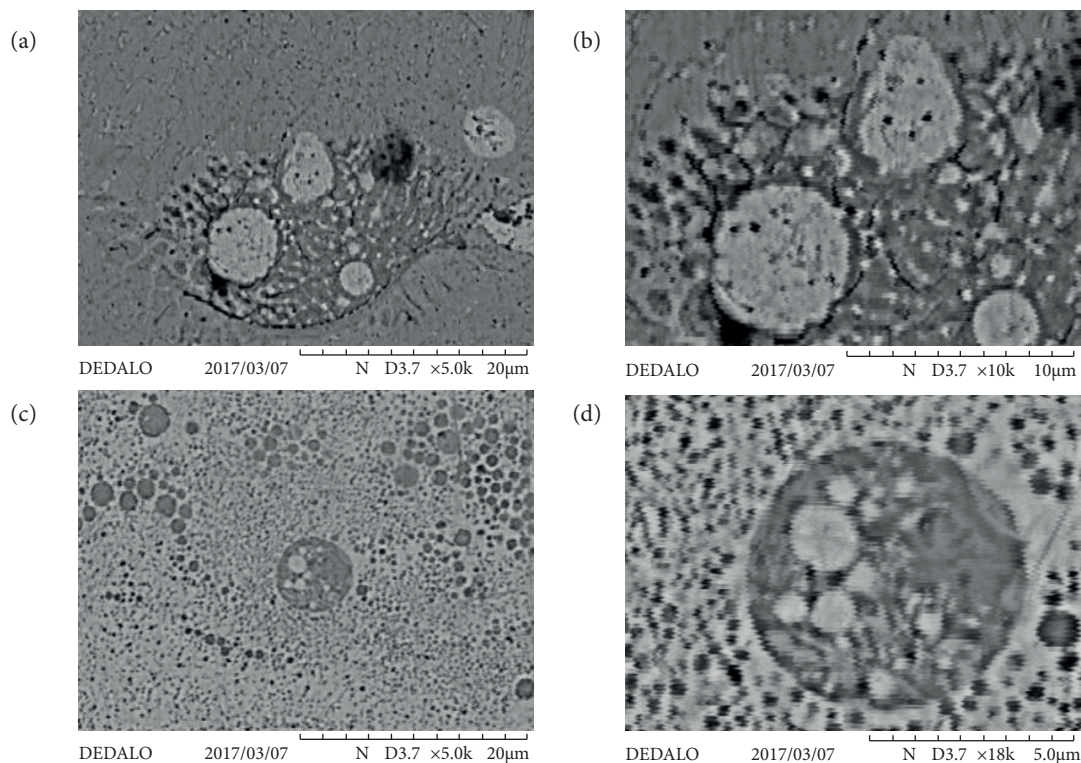
Figure 5. SEM microstructure of condition welding by 1600 W laser power and 1 m/min laser speed. (a) Flotting Cu globules in the iron melt region; (b) Fe-rich precipitates in solid-state inside Cu globulus; (c) Cu-rich regions; (d) Detailed Cu-rich precipitates in solid state inside Fe globulus.

CHEMICAL MODULATIONS

Although it is quite easy to observe Fe-rich and Cu-rich regions in the previous microstructural observations, it is necessary to quantify these heterogeneities using EDS measurements. As can be seen in Fig. 6, a given chemical profile in the middle of the weld for all conditions could be divided in three regions:

- A steel resolidified region up to 0.4 mm in depth from the upper surface;
- A mixture region between 0.4 and 1 mm in depth;
- A Cu-based resolidified region from 1 mm to the root of the weld.

The steel side region of the weld beads is of particular interest because this hot part exposed to the ambient atmosphere in a combustion chamber for rocket engine. The composition of the region was then evaluated using EDS-SEM, as presented in Fig. 7. As can be seen, the alloy produced has an approximated composition Fe-25%Cr-5%Ni-20%Cu with the largest range in Cu content. According to the FEDAT thermocalc database (Andersson *et al.* 2002), such composition will result in a solid with 64% ferrite, 19% austenite and 17% Cu. The residual copper will be more pure than the original sheet (Table 1) and the principal alloying element will be Ni (up to 1.3 %wt.). This phase segregation could be hazardous to the mechanical properties as long a line of residual Cu liquid could give rise to hot spots, as pointed out by Cheng *et al.* (2019).

Some cracks are born in the steel region, near to the top, which disagrees with the well-known good weldability of the AISI 304. A close look in the crack sensitive region shows some copper segregated to the interdendritic region (arrows in Fig. 8), which is responsible for hot spots. As Cu possesses a low melting point, compared to Fe, and because of the low solubility of Cu in the austenite, the small fraction of Cu dissolved in these regions remains liquid in the interdendritic spaces. Since the weld produced high tensile stresses near the end of steel solidification, these hot spots produce cracking due to the liquation issue.
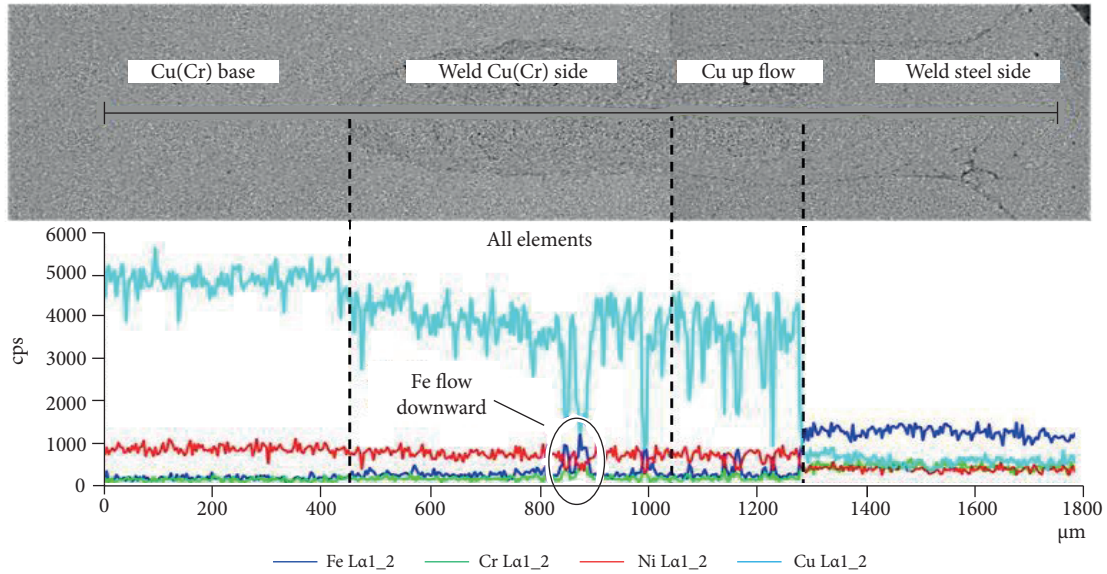
Figure 6. Line scan chemical profile of the weld 3 (Table 3).
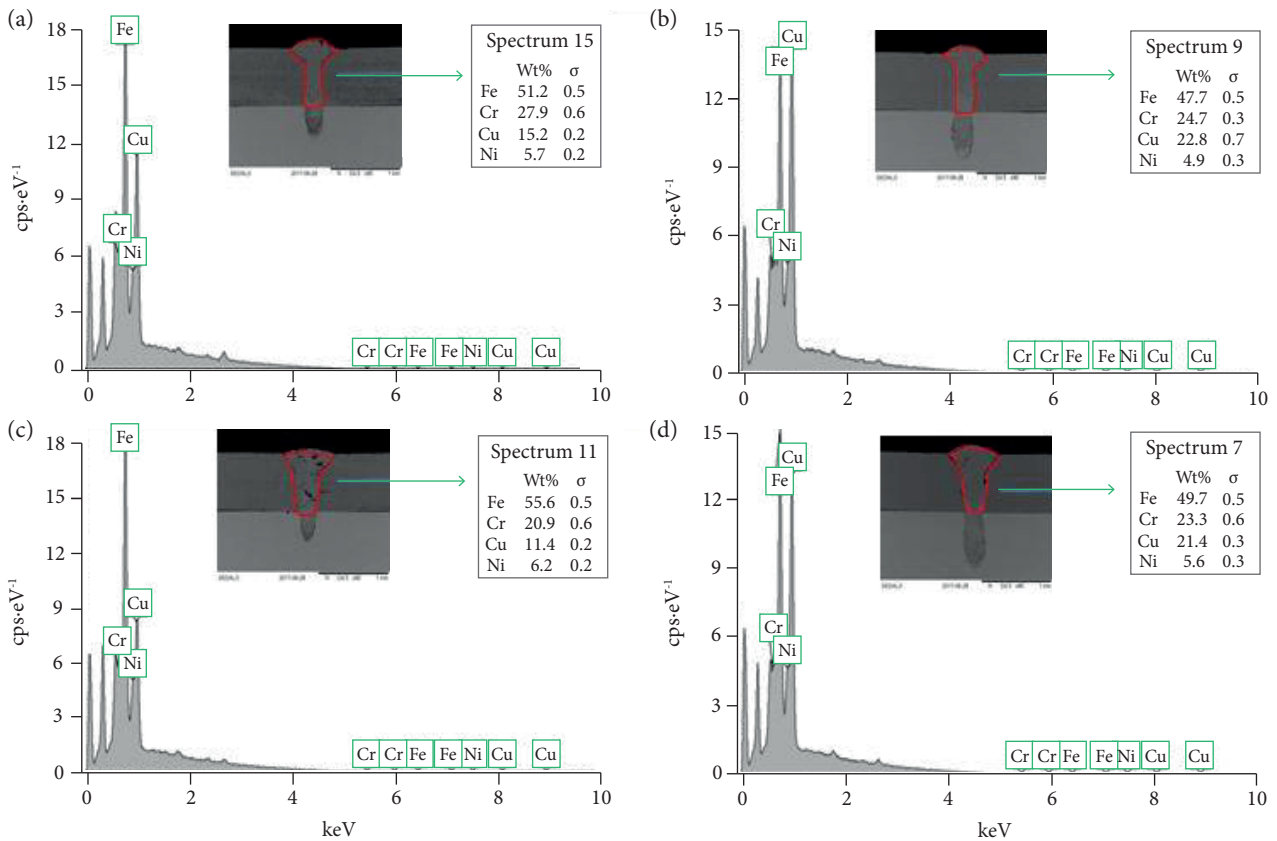

Figure 7. Chemical spectra of AISI 304 weld side for all weld condition: (a) 1200 W and 1m/min; (b) 1400 W and 1m/min; (c)1600 W and 1m/min; and (d) 1800 W and 1m/min.
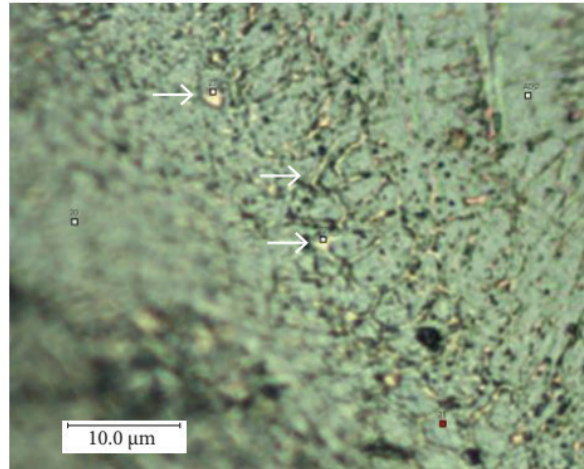
Figure 8. Cu segregation in the interdendritic spaces of iron region (arrows).

HARDNESS

The average hardnesses for both base materials are 120 HV (Cu C18200) and 190 HV (AISI 304L), as shown in Fig. 9. After laser welding, the hardness distribution profile was measured through the fusion zone with the same notation marked in Fig. 6. The hardness average at the top of the weld was 170 ± 10 HV, being slightly below the steel reference value. The high Cu contamination, up to 20%, corroborates this reduction. The Cu upflow zone and weld Cu(Cr) regions presented large HV values due to the phase separation in the liquid state with followed interglobular segregation (Fig. 5). Despite the chemical and microstructural changes the samples HV values (Fig. 9) are basically bounded by steel and Cu HV limits.
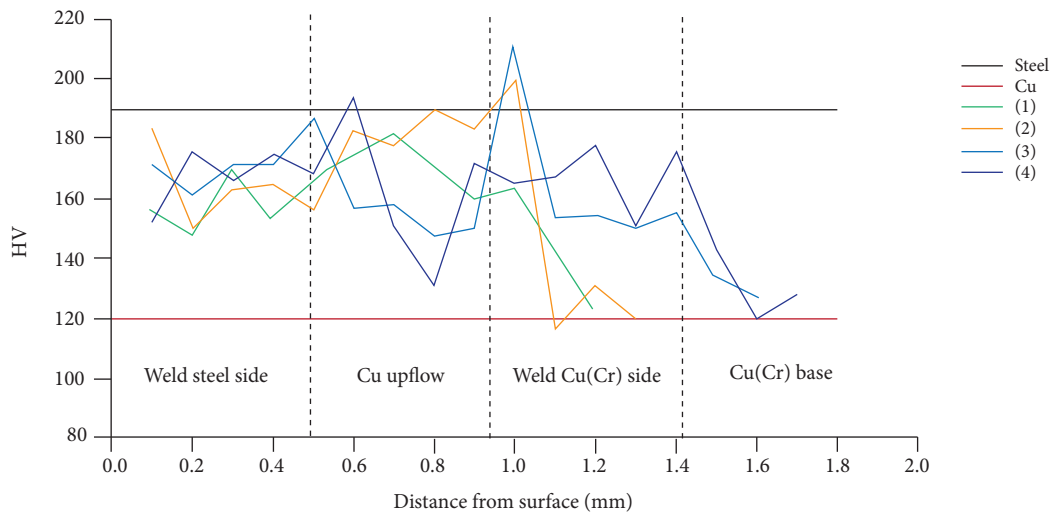

Figure 9. Hardness profiles across a fusion weld (top to bottom) produced by different laser power and weld speed of 1m/min. 1 = 1200 W; 2 = 1400 W; 3 = 1600 W; and 4 = 1800 W.

TENSILE STRENGTH

Figure 10 shows the load versus displacement curves of joint weld under condition 4. The tensile behavior was split in two curves, one load in the steel coupon (blue line) and one load in the Cu coupon (red line). As the tensile test specimen were overlapped, it was possible to distinguish two different behaviors depending on the interface toughness. Figure 10a shows that,

when the weld interface broke during load, all fusion weld broke as well (weld interface, Fe-rich and Cu-rich side). Which means that probably the crack grown up through the weld bead. On the other hand, Fig. 10b shows that first the interface weld broke and the materials kept straining, after same displacement copper weld broke, and lastly the stainless steel fractures by overloading. In this way, is possible to estimate the maximum shear stress for the interface weld as 330 MPa and 270 MPa, respectively, for Figs. 10a and 10b. The nominal ultimate tensile shear strength for copper C18200 and AISI 304 are 460 and 590 MPa, respectively. The strength of weld interface was almost 60% of Copper ultimate tensile strength.
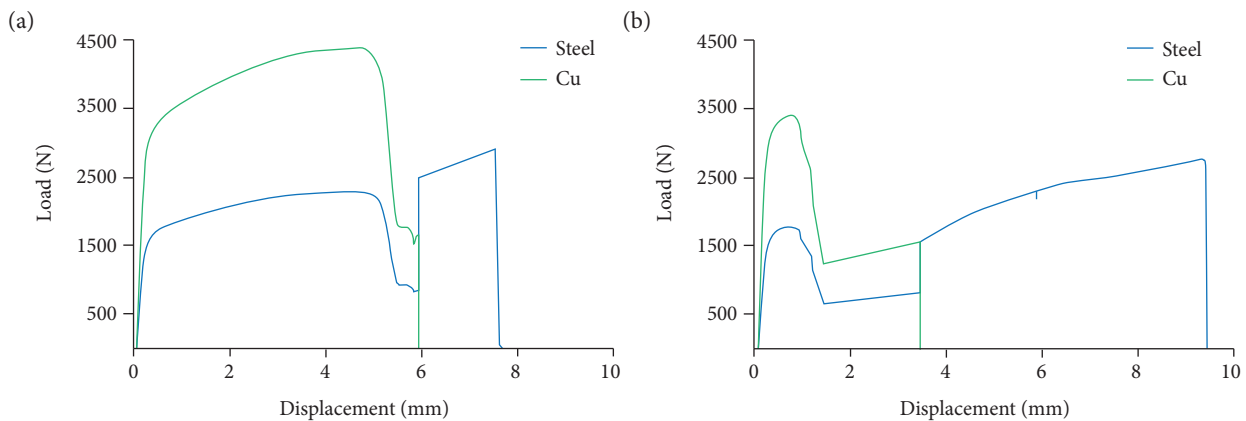
(a)   (b)

Figure 10. Load displacement curve for condition weld at 1600 W and 1 m/min. (a) Specimen 1 curve; (b) Specimen 2 curve.

CONCLUSIONS

The following conclusions could be drawn:

A 0.75 mm thick 304 stainless steel sheet was successfully joined to a 2.05 mm thick C18200 copper bar using a fiber laser. The welds were produced with an intensity between 3.8×10^4 and 5.7×10^4 W/mm^2 and a heat input between 72 and 108 J/mm, giving an aspect ratio of 1.8 and a melt depth between 0.6 and 0.7 mm.

The microstructure of the weld beads is marked by chemical heterogeneities due to the phase separation between Cu and Fe in the liquid state. The phase separation gave rise to globular precipitates that further transforms due to a secondary precipitation.

The steel side part of the welds presents around 20% Cu, contributing to a liquation of the grain boundaries and cracking. Hardness values situated between both base materials and the tensile behavior. When the weld is sufficiently tough it presents strength up to 590 MPa and elongation up to 9.5%.

AUTHORS' CONTRIBUTION

Conceptualization, Carvalho SM; Investigation, Carvalho SM and Siqueira RHM; Writing – Original Draft, Lima MSF; Writing – Review and Editing, Siqueira RHM; Supervision, Lima MSF.

ACKNOWLEDGMENTS

REFERENCES

Andersson JO, Helander T, Höglund L, Shi PF, Sundman B (2002) Thermo-calc and DICTRA, computational tools for materials science. Calphad 26(2):273-312. https://doi.org/10.1016/S0364-5916(02)00037-8

Chen S, Huang J, Xia J, Zhao X, Lin S (2015) Influence of processing parameters on the characteristics of stainless steel/copper laser welding. J Material Processing Technology 222:43-51. https://doi.org/10.1016/j.jmatprotec.2015.03.003

Cheng Z, Huang J, Ye Z, Chen Y, Yang J, Chen S (2019) Microstructures and mechanical properties of copper-stainless steel butt-welded joints by MIG-TIG double-sided arc welding. Journal of Materials Processing Tech 265:87-98. https://doi.org/10.1016/j.jmatprotec.2018.10.007

Kuryntsev SV, Morushkin AE, Gilmutdinov AK (2017) Fiber laser welding of austenitic steel and commercially pure copper butt joint. Optics and Lasers in Engineering 90:101-109. https://doi.org/10.1016/j.optlaseng.2016.10.008

Magnabosco I, Ferro P, Bonollo F, Arnberg L (2006) An investigation of fusion zone microstructures in electron beam welding of copper–stainless steel. Mater Sci Eng A 424(1-2):163-173. https://doi.org/10.1016/j.msea.2006.03.096

Mai TA, Spowage AC (2004) Characterisation of dissimilar joints in laser welding of steel–kovar, copper–steel and copper–aluminium. Mater Sci Eng A 374(1-2):224-233. https://doi.org/10.1016/j.msea.2004.02.025

Meng Y, Li X, Gao M, Zeng X (2019) Microstructures and mechanical properties of laser-arc hybrid welded dissimilar pure copper to stainless steel. Optics & Laser Technology 111:140-145. https://doi.org/10.1016/j.optlastec.2018.09.050

Munitz A (1995) Metastable liquid phase separation in tungsten inert gas and electron beam copper/stainless-steel welds. Journal of Materials Science 30(11):2901-2910. https://doi.org/10.1007/BF00349662

Noecker FF, DuPont JN (2007) Microstructural development and solidification cracking susceptibility of Cu deposits on steel: part ii-use of a Ni interlayer. Journal of Material Science 42(2):510-521. https://doi.org/10.1007/s10853-006-1259-1

Velu M, Bhat S (2015) Experimental investigations of fracture and fatigue crack growth of copper–steel joints arc welded using nickel-base filler. Materials & Design 67:244-260. https://doi.org/10.1016/j.matdes.2014.11.026

Wang HH, Tong Z, Hou TP, Wu KM, Mehmood T (2017) Effects of evolution of nanoscale copper precipitation and copper content on mechanical properties of high-strength steel weld metal. Science and Technology of Welding and Joining 22(3):191-197. https://doi.org/10.1080/13621718.2016.1213583